CORA Cork Open Research Archive
Cartlann Taighde Oscailte Chorcaí

Title	Efficient on-chip green light generation via frequency upconversion in SiN–transfer-printed LN hybrid waveguides
Authors	Sumon, Md. Saiful Islam;Vorobev, Artem S.;Ghosh, Samir;Atar, Fatih Bilge;Maraviglia, Nicola;Nikor, Sk. Shafaat Saud;Devarapu, Ganga Chinna Rao;Maddi, Chiranjeevi;Faruque, Imad I.;Dwivedi, Sarvagya;Bowman, Robert;O'Faolain, Liam;Corbett, Brian;Arafin, Shamsul
Publication date	2025-05-07
Original Citation	Sumon, M. S. I., Vorobev, A. S., Ghosh, S., Atar, F. B., Maraviglia, N., Nikor, S. S. S., Devarapu, G. C. R., Maddi, C., Faruque, I. I., Dwivedi, S. and Bowman, R., O'Faolain, L., Corbett, B. and Arafin, S. (2025) 'Efficient on-chip green light generation via frequency upconversion in SiN–transfer-printed LN hybrid waveguides', Optics Letters, 50(10), pp.3281-3284. https://doi.org/10.1364/OL.560034
Type of publication	Article (peer-reviewed);journal-article
Link to publisher's version	10.1364/ol.560034
Rights	© 2025, Optica Publishing Group. All rights reserved.
Download date	2026-11-06 03:57:01
Item downloaded from	https://hdl.handle.net/10468/17646

UCC
University College Cork, Ireland
Coláiste na hOllscoile Corcaigh

Efficient On-Chip Green Light Generation via Frequency Up-Conversion in SiN–Transfer-Printed LN Hybrid Waveguides

MD SAIFUL ISLAM SUMON,[1] ARTEM S. VOROBEV,[2,3] SAMIR GHOSH,[3] FATIH BILGE ATAR,[3] NICOLA MARAVIGLIA,[2,3] SK SHAFAAT SAUD NIKOR,[1] GANGA CHINNA RAO DEVARAPU,[2,3] CHIRANJEEVI MADDI,[4] IMAD I. FARUQUE,[5] SARVAGYA DWIVEDI,[6] ROBERT BOWMAN,[4] LIAM O'FAOLAIN,[2,3] BRIAN CORBETT,[3] AND SHAMSUL ARAFIN[1,*]

[1]*Department of Electrical and Computer Engineering, The Ohio State University, Columbus, Ohio 43210, USA*
[2]*Centre for Advanced Photonics and Process Analysis, Munster Technological University, T12 T66T Bishopstown, Cork, Ireland*
[3]*Tyndall National Institute, University College Cork, Lee Maltings Complex, Dyke Parade, T12 R5CP Cork, Ireland*
[4]*School of Mathematics and Physics, Queen's University Belfast, Belfast, BT7 1NN, UK*
[5]*School of Mathematical and Physical Science, University of Sheffield, S3 7RH Sheffield, UK*
[6]*Kilby Labs, Texas Instruments, Dallas, Texas 75243, USA*
*arafin.1@osu.edu

Received XX Month XXXX; revised XX Month, XXXX; accepted XX Month XXXX; posted XX Month XXXX (Doc. ID XXXXX); published XX Month XXX

We demonstrate efficient on-chip green light generation via frequency up-conversion in silicon nitride-thin film lithium niobate (SiN-TFLN) hybrid waveguides, obtained by transfer printing LN coupons on selected areas of photonic integrated circuits (PICs). By utilizing modal phase matching (MPM), our devices achieve a high normalized conversion efficiency of 42.5% $W^{-1}cm^{-2}$ in a single-pass, 2.4 mm-long waveguide configuration. The SiN-LN transition in the waveguide inherently facilitates mode conversion, transforming a higher-order second-harmonic mode into a fundamental TE mode, ensuring coherent, narrow-linewidth, green light emission. Our waveguide platform gives rise to a wavelength shift of ~1 nm for every 10 nm of waveguide width variation and temperature-induced wavelength tuning at ~0.02 nm/°C.

Introduction. Visible light, particularly at green wavelengths, is crucial for diverse applications, including biomedical imaging [1], health monitoring [2], satellite communication [3], and quantum technologies [4]. However, traditional optical systems for green light generation and related applications are often bulky, expensive, and unsuitable for compact integration. Photonic integrated circuits (PICs) offer a transformative solution, enabling the miniaturization and cost-effective integration of optical systems at the chip scale. To date, the development of compact chip-scale and efficient coherent green-yellow light sources remains a major challenge due to the well-known green gap [5]. Semiconductor diode lasers based on InGaN alloys with high indium content are a promising approach for direct green light generation. However, their performance is constrained by maximum achievable wavelength, linewidth, stability, and overall efficiency [6]. To overcome these limitations, frequency up-conversion techniques such as second-harmonic generation (SHG) could be one of the potential solutions, to convert near-infrared (NIR) pump light into green light [7–9]. Lithium niobate (LN), known for its exceptional nonlinear properties, is an ideal material for frequency conversion due to its high nonlinear coefficient and broad optical transparency window [10,11]. The development of thin-film LN (TFLN) on insulators has further enhanced its compatibility with integrated photonics, enabling strong light confinement and efficient nonlinear interactions in compact waveguides [12,13].

Among phase-matching techniques, MPM has emerged as an efficient and versatile solution for SHG [14–19]. While quasi-phase matching (QPM) enables strong nonlinear interactions through periodic poling, MPM achieves phase matching by utilizing waveguide modal properties, eliminating the complexity associated with domain inversion while maintaining a high conversion efficiency [15]. Previous studies have demonstrated efficient SHG using MPM in LN-based waveguides and resonant cavities [14,16–19], but most approaches rely on TFLN ridge formation with etched sidewalls being the part of the waveguides, limiting compatibility with silicon and SiN platforms and scalability for diverse applications.

This study introduces an emerging SiN-LN hybrid waveguide platform for green light generation, which were explored for various photonic applications including high-speed modulators [20], micro-ring resonators [21], large-scale heterogeneous integration [22], tunable filters [23], and nonlinear optical processes [24,25] at 1550 nm. Leveraging the low-loss and well-established SiN platform, this approach selectively integrates LN only in regions where frequency conversion is required, utilizing micro-transfer printing and alleviating the deleterious effect of sidewall roughness associated with LN etching [26]. While initial design and fabrication efforts have explored similar concepts [26,27], we demonstrate SHG from transfer-printed LN on SiN

waveguides for the first time. By employing type-0 MPM between the fundamental (FF) TE_{00} pump mode and the higher-order second harmonic (SH) TE_{01} mode, our single-pass waveguide devices achieve a normalized conversion efficiency of 42.5% $W^{-1}cm^{-2}$ for the 2.4 mm-long SiN-LN hybrid waveguides. The measured SHG efficiency only considers the conversion from FF TE_{00} to SH TE_{01}, while the subsequent conversion from SH TE_{01} to SH TE_{00} represents an additional loss after the green light generation. The transition between the hybrid SiN-LN waveguide to the bare SiN waveguide inherently converts the TE_{01} green mode into a fundamental TE_{00} output with a calculated efficiency of nearly 70%, delivering the most practical output mode for downstream photonic devices and applications. Phase-matched SHG wavelengths can be pre-set by waveguide width as a design parameter and fine-tuned by chip temperature, allowing flexible and precise control of green wavelengths. Such a platform offers a scalable solution for green light generation and holds the potential for a broad spectrum of nonlinear photonic applications, including spontaneous parametric down-conversion and modulation [28,29].

Design. The hybrid SiN-LN (*x*-cut, *y*-propagating) waveguide was designed in this work. The waveguide consists of four regions: (i) an input SiN waveguide, (ii)-(iii) a hybrid SiN-LN waveguide, and (iv) an output SiN waveguide, as shown in Fig. 1(a). A 300 nm LN film on a

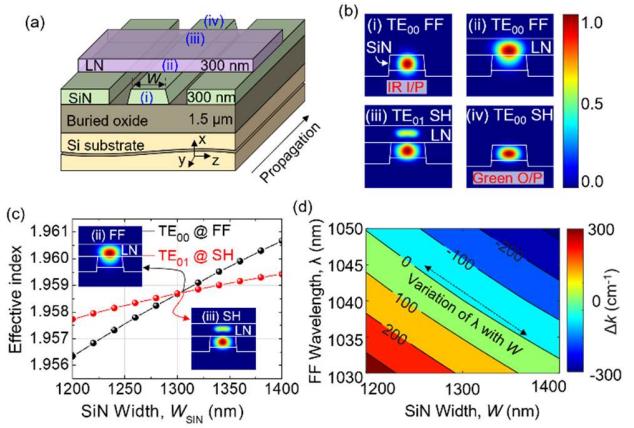


Fig. 1. Design of the SiN-LN hybrid waveguide for SHG. (a) Schematic of the proposed single-pass SHG waveguide showing the input SiN waveguide (i), hybrid SiN-LN waveguide regions (ii)-(iii), and output SiN waveguide (iv). (b) Mode profiles of the TE_{00} pump mode in regions (i)-(ii), the TE_{01} SH mode in region (iii), and the TE_{00} SH mode at the output (iv). IR I/P: infrared input at 1040 nm, Green O/P: green output at 520 nm. (c) dispersion curves of the fundamental and SH modes to get MPM. Inset: the corresponding modes. (d) phase mismatch contour plot (Δk) showing tunability of the mode-matching wavelength by varying waveguide width.

300-nm-thick SiN ridge formed the hybrid region, ensuring compatibility with silicon photonics. Mode profiles for the 1040 nm pump and 520 nm SH are shown in Fig. 1(b). In region (i), the input SiN waveguide supports the fundamental transverse electric (TE_{00}) mode of the NIR pump laser. As the mode propagates into the SiN-LN hybrid region (ii)-(iii), it remains in TE_{00} but shifts into the LN layer due to its higher refractive index, ensuring enhanced nonlinear interactions. In region (iii), SHG occurs and the higher-order TE_{01} mode at green wavelengths is generated. At the output SiN waveguide (iv), the TE_{01} mode is efficiently converted back to the fundamental TE_{00} mode, facilitated by ~70% mode overlap and negligible back reflection due to the low refractive index contrast at the SiN-LN interface. While this overlap can be further enhanced by tapering [29], the inherent mode conversion eliminates the need for additional mode converters, ensuring that the output maintains a fundamental TE_{00} mode with coherence matching that of the pump.

The efficient MPM-based frequency doubling design is illustrated in Fig. 1(c). Phase matching at 1040 nm → 520 nm is achieved by aligning the dispersion curves of the FF and SH modes, requiring a waveguide width of ~1300 nm. The effective mode area (2.1 μm²) and spatial mode overlap (0.27), between the FF and SH modes shown in Fig. 1(c) inset, yield a theoretical normalized conversion efficiency of 968%$W^{-1}cm^{-2}$, leveraging the highest nonlinearity of LN ($d_{eff} = d_{33} = 27$ pm/V) [30]. Calculations are based on [14]. The contour plot in Fig. 1(d) illustrates the dependence of phase mismatch Δk on waveguide width and pump wavelength. By varying the hybrid waveguide width from 1200 nm to 1400 nm, the mode-matching wavelength ($\Delta k = 0$) shifts from 1030 nm to 1050 nm, corresponding to SH wavelengths from 515 nm to 525 nm. This provides a design flexibility of ~1 nm shift in SHG wavelength per 10 nm change in waveguide width, allowing control over the generated green light.

Fabrication. Fabrication began with a commercially available SiN wafer [31], consisting of a 300 nm SiN layer on 1.5 μm of silicon dioxide (SiO_2), supported by a 525 μm silicon (Si) substrate. Waveguides were patterned via electron beam lithography with ZEP photoresist, followed by dry etching (CHF_3:O_2) to define SiN ridges. Waveguides presented a sidewall angle of ~81°. To properly defined the feature of interest, vertical etching was extended for an additional ~100 nm into buried oxide (BOX). Fig. 2 illustrates

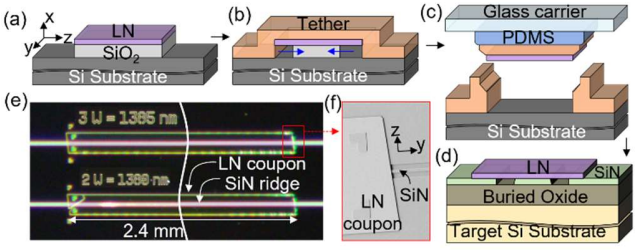


Fig. 2. Fabrication and integration of LN coupons onto SiN waveguides: (a) LN coupon prep on x-cut LNOI with 300 nm LN and 2 μm BOX layer. (b) Resist tethers secure coupon during BOX undercut. (c) PDMS stamp lifts LN coupon. (d) Coupon aligned and transferred to SiN ridge. (e) Optical image of LN on SiN ridges (two widths). (f) SEM image showing successful integration and alignment.

the integration of LN coupons into the SiN platform via micro-transfer printing. The LN coupons (2400 µm × 100 µm) were prepared from commercial x-cut LNOI wafers [32] with a 300 nm LN layer atop a 2 µm BOX layer. The BOX layer served as a release layer during coupon preparation from the patterned LN (Fig. 2a). A resist tether secured the LN coupon while undercutting the BOX with buffered oxide etchant (Fig. 2b). Using a polydimethylsiloxane (PDMS) stamp mounted on a glass carrier, the LN coupon was lifted from its substrate (Fig. 2c) and aligned onto the SiN ridge, forming the hybrid SiN-LN waveguide (Fig. 2d). The optical image in Fig. 2(e) confirms successful LN coupon integration along SiN ridges of different widths, while SEM imaging (Fig. 2f) validated precise alignment. This micro-transfer printing approach simplifies fabrication and ensures compatibility with silicon photonics workflows. The resulting SiN-LN hybrid waveguide provides a scalable platform for compact PICs paving the way for advanced nonlinear photonic applications.

Results. The experimental setup, schematically shown in Fig. 3(a), consists of a tunable NIR laser source with an

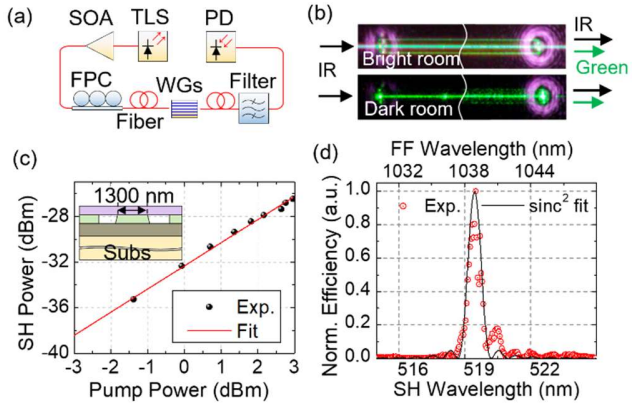


Fig. 3. SHG in SiN-LN hybrid waveguides. (a) Experimental setup with a tunable NIR laser (TLS), SOA, FPC, tapered fibers, IR filter, and VIS-IR detector (PD). (b) Green light generation under bright and dark conditions at the hybrid waveguide. (c) Quadratic SH power dependence on pump power, matching theoretical fit. Inset: 1300 nm-wide SiN-LN hybrid waveguide. (d) Normalized SH efficiency vs. wavelength with a sinc^2 fit, confirming phase matching. TLS: Tunable Laser Source, SOA: Semiconductor Optical Amplifier, PD: Photodetector, FPC: Fiber Polarization Controller, WGs: Waveguides.

amplifier, followed by a fiber polarization controller. The light is coupled into and out of the chip using tapered fibers of 2 µm mode field diameter, with the output signal passing through an IR filter before being detected by a VIS-IR detector. The calculated coupling losses for the FF TE_{00} and SH TE_{00} modes are approximately 3.2 dB and 6.2 dB, respectively. Experimental results confirm the successful generation of green light through second harmonic generation in SiN-LN hybrid waveguides. Fig. 3(b) illustrates the green light generation when pumped with a 1040 nm infrared laser, visible under both bright and dark room conditions. The emission, localized exclusively at the hybrid waveguide section, validates the design's effectiveness. Fig. 3(c) illustrates the dependence of SH power on input pump power at 25°C with a pump wavelength of 1040 nm. The experimental data align closely with the theoretical quadratic fit, demonstrating efficient nonlinear frequency conversion. The waveguide, with a 1300 nm top width with a sidewall angle of 81°(inset), achieved a normalized conversion efficiency, η of 42.5% $W^{-1}cm^{-2}$ for the conversion of 1040 nm to 520 nm, calculated using the formalism outlined in [14] for single-pass SHG devices. We primarily attribute the discrepancy between experimental and theoretical efficiency to abrupt SiN-hybrid waveguide interfaces, which induce deviations from the designed fundamental and second-harmonic modes.

Additional contributing factors include fabrication-induced width variations, slight angular misalignment of the LN coupon relative to the y-propagation direction, which affects mode matching along the propagation length, and propagation losses—particularly significant for the higher-order, lossy second-harmonic mode. Among these, the most critical variable is the waveguide width whose even small variations degrade the SHG performance compared to a uniform width along the propagation length. In contrast, deviations in sidewall angle, etch depth, and LN coupon placement angle within standard fabrication limits tend to have a lesser impact on the SHG performance. The propagation loss of the fundamental TE_{00} mode was reported to be <1 dB/cm at 1550 nm [33] for the same SiN transfer-printed LN platform, and we expect a similar value for our work at 1040 nm. The loss measurement of SH TE_{01} modes is challenging as it is internally generated within the waveguides. Hence, the loss values for both the modes are not yet accurately known and loss measurements will be performed in our future research. Engineering the waveguides to achieve a smooth transition of the modes from SiN to the hybrid waveguide and vice versa can significantly enhance overall performance, along with improvements in fabrication and other contributing factors. Wavelength-dependent SHG efficiency is presented in Fig. 3(d) at 25°C. A sinc-squared fit (black line) of the experimental normalized conversion efficiency (red circles) demonstrates a strong agreement between the experimental data and theoretical expectations. For a 2.4 mm-long waveguide, a conversion efficiency of 2.4 $\%W^{-1}$ with a 3 dB bandwidth of 0.8 nm is observed. Theoretically, SHG efficiency increases quadratically with waveguide length, suggesting better performance at longer lengths. However, propagation loss—particularly for the SH TE_{01} mode—limits this advantage in practice after a certain waveguide length. Although efficiency could be further enhanced by incorporating cavity structures such as ring resonators or Fabry-Perot cavities [18,19,27,34], the primary focus here is to demonstrate the effectiveness of the proposed hybrid platform based on micro-transfer printed LN for SHG using a single-pass waveguide structure.

Temperature-dependent wavelength tuning is demonstrated in Fig. 4(a), where SH spectra at the phase-matched wavelengths, recorded at 25°C (black), 50°C (red), and 75°C

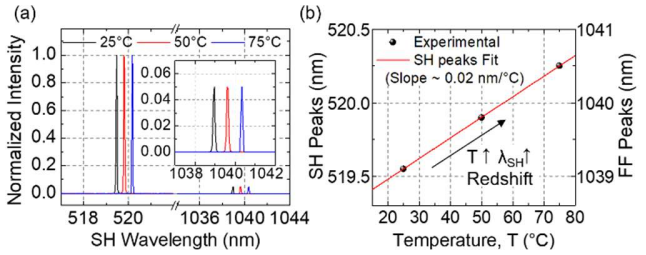


Fig. 4. Temperature-dependent second-harmonic (SH) wavelength shift. (a) SH spectra at 25°C (black), 50°C (red), and 75°C (blue), showing a redshift in mode matching wavelength with increasing temperature. Inset: zoomed-in view of filtered fundamental peaks. (b) SH peak shift (λ_{SH}) vs. temperature. Experimental data (black dots) and fit (red line) showing a slope of ~0.02 nm/°C, attributed to the temperature-dependent refractive index variation.

(blue), exhibit a clear redshift in peak position with increasing temperature. The inset in Fig. 4(a) shows the filtered infrared (IR) pump spectra at the output, corresponding to phase-matching pump wavelengths at different temperatures. Fig. 4(b) quantifies this shift, revealing a linear phase-matching dependence with a slope of ~0.02 nm/°C, attributed to temperature-dependent refractive index variation. While the tunability is constrained by the chosen FF and SH modes, it provides valuable flexibility for integrating wavelength-sensitive on-chip devices such as lasers, filters, and cavities, while also confirming the susceptibility of wavelength shifts to minor room-temperature variations. These results highlight the scalability, tunability, and high performance of the SiN-LN hybrid waveguide platform, reinforcing its potential for compact nonlinear photonic devices. To contextualize our results, we compare our type-0 MPM-based SHG in SiN-LN hybrid waveguides with studies for green light generation with single-pass configurations, as summarized in Table 1.

Table 1. Single-pass devices with MPM/BPM for green light generation

Mode Matching	Waveguide Wavelengths (nm)	Max η ($\%W^{-1}cm^{-2}$)	Year/Ref
Type-I/II	z-cut LNOI ridge 1018 to 509	0.12	2017 [35]
Type-I	z-cut LNOI ridge 1064 to 532	37	2024 [17]
Type-0 (This work)	x-cut LN-SiN hybrid 1040 to 520	42.5	2025

Type-I/II MPM in z-cut LNOI ridge waveguides, achieving a maximum normalized conversion efficiency of $0.12\%W^{-1}cm^{-2}$ for 1018 nm to 509 nm SHG were reported [28]. More recently, type-I birefringent phase matching (BPM) was employed, which is the same as MPM in *z*-cut lithium niobate waveguides for 1064 nm to 532 nm conversion, reaching $37\%W^{-1}cm^{-2}$ [17]. In our work, we utilize type-0 MPM in *x*-cut LN and achieve a record-high conversion efficiency of $42.5\%W^{-1}cm^{-2}$ for 1040 nm to 520 nm conversion. This efficiency can be further enhanced by optimizing factors such as the coupling between the SiN and hybrid regions. This enhancement over previous demonstrations is driven by optimized mode overlap, reduced effective area, strong χ^2 nonlinearity (d_{33}), and precise SiN-LN hybrid integration. These results highlight the advantage of type-0 MPM in achieving high-efficiency SHG while maintaining a scalable and fabrication-compatible platform for integrated nonlinear photonics.

Conclusion. This work demonstrates efficient on-chip green light generation via frequency up-conversion in SiN-LN hybrid waveguides using type-0 MPM. The transfer-printed LN integration enables a scalable, compact, and high-performance platform for visible-light photonics and nonlinear optical applications. A normalized efficiency of $42.5\%W^{-1}cm^{-2}$ is achieved in a 2.4 mm-long waveguide. The device showed thermal tunability (~0.02 nm/°C) and a 3 dB bandwidth of 0.8 nm, with inherent TE_{01}-to-TE_{00} mode conversion. This work lays the foundation for visible-wavelength PICs, with future efforts aimed at integrating on-chip NIR lasers, enhancing coupling, and adding Fabry-Pérot and ring cavities for efficient green light generation.

Funding. This work was supported by the National Science Foundation (NSF), USA under Grant #2310869, Research Ireland SFI-22/US/3834, and the Dept for the Economy Northern Ireland under the US-Ireland R&D Partnership Programme.

Disclosures. The authors declare no conflicts of interest.

Data Availability. Data underlying the results presented in this paper are not publicly available at this time but may be obtained from the authors upon reasonable request.

REFERENCES

1. C. E. Badr and B. A. Tannous, Trends Biotechnol. 29, 624 (2011).
2. T. Tamura, Biomed. Eng. Lett. 9, 21 (2019).
3. E. Ciaramella, G. Cossu, E. Ertunc, et al., ICTON, 1 (2020).
4. R. Zia-Ul-Mustafa, S. S. Boroujeni, C. Guerra-Yanez, et al., CSNDSP, 589 (2022).
5. T. D. Moustakas and R. Paiella, Rep. Prog. Phys. 80, 106501 (2017).
6. K. Kishimoto, T. Hirao, T. Morizumi, et al., SPIE Gallium Nitride Mater. Devices XIX 12886, 41 (2024).
7. D. A. Kleinman, Phys. Rev. 128, 1761 (1962).
8. A. Aghigh, S. Bancelin, M. Rivard, et al., Biophys. Rev. 15, 43 (2023).
9. E. J. Lim, M. M. Fejer, and R. L. Byer, Electron. Lett. 25, 174 (1989).
10. K. K. Wong, ed., Properties of Lithium Niobate, IET 28 (2002).
11. L. Arizmendi, Phys. Status Solidi A 201, 253 (2004).
12. Y. Zheng and X. Chen, Adv. Phys. X 6, 1889402 (2021).
13. M. G. Vazimali and S. Fathpour, Adv. Photonics 4, 034001 (2022).
14. R. Luo, H. Jiang, H. Liang, et al., Optica 5, 1006 (2018).
15. M. L. Jäger, M. Wegener, S. Linden, et al., MRS Online Proc. Libr. 488, 179 (1997).
16. I. Briggs, S. Hou, C. Cui, et al., Opt. Express 29, 26183 (2021).
17. T. Ding, Y. Tang, H. Li, et al., Opt. Lett. 49, 1121 (2024).
18. R. Luo, H. Jiang, S. Rogers, et al., Opt. Express 25, 24531 (2017).
19. R. Luo, Y. He, H. Liang, et al., Phys. Rev. Appl. 11, 034026 (2019).
20. T. Vanackere, T. Vandekerckhove, L. Bogaert, et al., APL Photonics 8 (2023).
21. Z. Li, J. A. Smith, M. Scullion, et al., Opt. Mater. Express 12, 4375 (2022).
22. M. Niels, T. Vanackere, T. Vandekerckhove, et al., Opt. Mater. Express 15, 531 (2025).
23. J. Su, W. Gao, Z. Cui, et al., ACP/IPOC, 1 (2024).
24. T. Vanackere, T. Vandekerckhove, M. Billet, et al., Integr. Photonics Platforms III, SPIE, 13012, 58 (2024).
25. M. Churaev, R. N. Wang, A. Riedhauser, et al., Nat. Commun. 14, 3499 (2023).
26. A. Ananthachar, M. Kotlyar, S. Ghosh, et al., Integr. Photonics Res., IM3B-6 (2022).
27. M. S. I. Sumon, S. Sankar, I. I. Faruque, et al., CLEO, 1 (2024).
28. C. Couteau, Contemp. Phys. 59, 291 (2018).

29. F. Valdez, V. Mere, and S. Mookherjea, Optica 10, 578 (2023).
30. D. A. Roberts, IEEE J. Quantum Electron. 28, 2057 (1992).
31. https://www.lionix-international.com/
32. https://www.nanoln.com/
33. M. Niels, T. Vanackere, S. Poelman, et al., CLEO-PR, 1 (2024).
34. M. V. Kotlyar, S. Iadanza, and L. O'Faolain, Photonics Nanostruct. 43, 100886 (2021).
35. C. Zhu, Y. Chen, G. Li, et al., Chin. Opt. Lett. 15, 091901 (2017).

REFERENCES

1. C. E. Badr and B. A. Tannous, "Bioluminescence imaging: progress and applications," Trends Biotechnol. 29(12), 624–633 (2011).
2. T. Tamura, "Current progress of photoplethysmography and SPO2 for health monitoring," Biomed. Eng. Lett. 9(1), 21–36 (2019).
3. E. Ciaramella, G. Cossu, E. Ertunc, L. Gilli, A. Messa, M. Presi, M. Rannello, F. Bresciani, V. Basso, R. Dell'Orso, and F. Palla, "Prospects of visible light communications in satellites," 22nd Int. Conf. Transparent Opt. Netw. (ICTON), 2020, 1–4 (July 2020).
4. R. Zia-Ul-Mustafa, S. S. Boroujeni, C. Guerra-Yanez, et al., "Quantum Key Distribution for Visible Light Communications: A Review," Proc. Int. Symp. Commun. Syst. Netw. Digit. Signal Process. (CSNDSP), 589–594 (2022).
5. T. D. Moustakas and R. Paiella, "Optoelectronic device physics and technology of nitride semiconductors from the UV to the terahertz," Rep. Prog. Phys. 80(10), 106501 (2017).
6. K. Kishimoto, T. Hirao, T. Morizumi, et al., "Development of highly efficient blue and green edge-emitting laser diodes," Proc. SPIE Gallium Nitride Mater. Devices XIX 12886, 41–46 (2024).
7. D. A. Kleinman, "Theory of second harmonic generation of light," Phys. Rev. 128(4), 1761 (1962).
8. A. Aghigh, S. Bancelin, M. Rivard, et al., "Second harmonic generation microscopy: a powerful tool for bio-imaging," Biophys. Rev. 15(1):43–70 (2023).
9. E. J. Lim, M. M. Fejer, and R. L. Byer, "Second-harmonic generation of green light in periodically poled planar lithium niobate waveguide," Electron. Lett. 25(3), 174–174 (1989).
10. K.K. Wong, ed., Properties of Lithium Niobate, IET 28, (2002).
11. L. Arizmendi, "Photonic applications of lithium niobate crystals," Phys. Status Solidi A 201(2), 253–283 (2004).
12. Y. Zheng and X. Chen, "Nonlinear wave mixing in lithium niobate thin film," Adv. Phys. X 6(1), 1889402 (2021).
13. M. G. Vazimali and S. Fathpour, "Applications of thin-film lithium niobate in nonlinear integrated photonics," Adv. Photonics 4(3), 034001 (2022).
14. R. Luo, H. Jiang, H. Liang, et al., "Highly tunable efficient second-harmonic generation in a lithium niobate nanophotonic waveguide," Optica 5(8), 1006–1011 (2018).
15. M. L. Jäger, M. Wegener, S. Linden, et al., "Advantages of Modal Dispersion Phase-Matching and Materials Requirements for Polymeric Devices Using Efficient Second Harmonic Generation at Telecommunication Wavelength," MRS Online Proc. Libr. 488, 179–191 (1997).
16. I. Briggs, S. Hou, C. Cui, et al., "Simultaneous type-I and type-II phase matching for second-order nonlinearity in integrated lithium niobate waveguide," Opt. Express 29(16), 26183–26190 (2021).
17. T. Ding, Y. Tang, H. Li, et al., "Noncritical birefringence phase-matched second harmonic generation in a lithium-niobate-on-insulator micro-waveguide for green light emission," Opt. Lett. 49(5), 1121–1124 (2024).
18. R. Luo, H. Jiang, S. Rogers, et al., "On-chip second-harmonic generation and broadband parametric down-conversion in a lithium niobate microresonator," Opt. Express 25(20), 24531–24539 (2017).
19. R. Luo, Y. He, H. Liang, et al., "Optical parametric generation in a lithium niobate microring with modal phase matching," Phys. Rev. Appl. 11(3), 034026 (2019).
20. T. Vanackere, T. Vandekerckhove, L. Bogaert et al., "Heterogeneous integration of a high-speed lithium niobate modulator on silicon nitride using micro-transfer printing," APL Photonics 8(8) (2023).
21. Z. Li, J. A. Smith, M. Scullion et al., "Photonic integration of lithium niobate micro-ring resonators onto silicon nitride waveguide chips by transfer-printing," Opt. Mater. Express 12(11), 4375–4383 (2022).
22. M. Niels, T. Vanackere, T. Vandekerckhove et al., "Centimetre-scale micro-transfer printing to enable heterogeneous integration of thin film lithium niobate with silicon photonics," Opt. Mater. Express 15(3), 531–540 (2025).
23. J. Su, W. Gao, Z. Cui et al., "Narrowband fast-tunable microring filter based on micro-transfer printed thin-film lithium niobate on silicon nitride," 2024 Asia Communications and Photonics Conference (ACP) and International Conference on Information Photonics and Optical Communications (IPOC), 1–4 (2024).
24. T. Vanackere, T. Vandekerckhove, M. Billet et al., "Towards scalable heterogeneous integration of thin-film lithium niobate on silicon photonics using micro-transfer printing," Integrated Photonics Platforms III, SPIE, 13012, 58–62 (2024)
25. M. Churaev, R. N. Wang, A. Riedhauser et al., "A heterogeneously integrated lithium niobate-on-silicon nitride photonic platform," Nat. Commun. 14(1), 3499 (2023)
26. A. Ananthachar, M. Kotlyar, S. Ghosh, et al., "Realization of a micro-cavity via the integration of Silicon Nitride and Lithium Niobate using micro transfer printing," Proc. Integr. Photonics Res., Silicon Nanophotonics, IM3B-6 (2022).
27. M. S. I. Sumon, S. Sankar, I. I. Faruque, et al., "Enhanced On-Chip Green Light Generation by Nonlinear Up-Conversion Using Fabry-Pérot Microcavities," Conf. Lasers Electro-Optics (CLEO), 1–2 (2024).
28. C. Couteau, "Spontaneous parametric down-conversion," Contemp. Phys. 59(3), 291–304 (2018).
29. F. Valdez, V. Mere, and S. Mookherjea, "100 GHz bandwidth, 1 volt integrated electro-optic Mach–Zehnder modulator at near-IR wavelengths," Optica 10(5), 578–584 (2023).
30. D. A. Roberts, "Simplified characterization of uniaxial and biaxial nonlinear optical crystals: a plea for standardization of nomenclature and conventions," IEEE J. Quantum Electron. 28(10), 2057–2074 (1992).
31. https://www.lionix-international.com/
32. https://www.nanoln.com/
33. M. Niels, T. Vanackere, S. Poelman et al., "Characterisation of micro-transfer printed cm-scale lithium niobate on a silicon nitride platform," 2024 Conference on Lasers and Electro-Optics Pacific Rim (CLEO-PR), 1–3 (2024)
34. M. V. Kotlyar, S. Iadanza, and L. O'Faolain, "Lithium Niobate Fabry-Perot microcavity based on strip-loaded waveguides," Photonics Nanostruct. - Fundam. Appl. 43, 100886 (2021).
35. C. Zhu, Y. Chen, G. Li, et al., "Multiple-mode phase matching in a single-crystal lithium niobate waveguide for three-wave mixing," Chin. Opt. Lett. 15(9), 091901 (2017).